

MICRO-PIV INVESTIGATION OF A SINUSOIDAL CROSSFLOW MICROFILTRATION MODULE

Michal M. Mielnik, michalm@mtf.ntnu.no
Lars R. Sætran, larssa@mtf.ntnu.no

Department of Energy and Process Technology
Norwegian University of Science and Technology
7491 Trondheim, Norway

ABSTRACT

A micro-PIV system is presented in detail, pointing out important aspects of micro-PIV system design crucial for its operation. The micro-PIV system is then applied on a sinusoidal microchannel, and the fluid motion inside the device is presented and discussed. The wall shear stress at the waist of the channel is measured to be up to 60% higher than the wall shear stress in a conventional parallel-plate flow. The results suggest that altering of channel geometry may contribute to better design of cross-flow microfiltration units, in terms of reduced clogging by shear-control of bacterial motion. Furthermore, the flow is shown to exhibit a strong Reynolds number dependence, characterised by the onset of periodic distortion imposed on the flow by the sinusoidal walls occurring between $Re=2$ and $Re=10$.

INTRODUCTION

Filtration of particles, such as blood- or bacteria cells, is an important and unresolved issue in many bio-MEMS applications. In crossflow filtration, the cell suspension to be filtered flows through a channel with one or more porous walls. Due to a pressure difference between the fluid inside the channel and the reservoir outside, the Trans Membrane Pressure (TMP), the fluid permeates through the membrane while the cells remain within the bulk flow and emerge in a more concentrated form at the exit of the crossflow filtration module. The retentate may then be processed or recycled through the filtration module in order to achieve higher cell concentration.

The crossflow filtration method, although significantly better than conventional dead-end filtration, suffers from permeate flux reduction with time due to

formation of a clogging cell cake on the channel wall surfaces, even at constant mass flow conditions (Caridis and Papathanasiou, 1997).

For small pressure differences (TMP), the permeate flux increases with increasing pressure. After reaching some critical value, however, the permeate flux tends to decrease due to growth of cell cake on the membrane. Caridis and Papathanasiou (1997) compare critical values of TMP found by various authors. These values range from 4 kPa to 250 kPa depending on membrane pore size and the cell species to be filtered. Although the reported results reveal some discrepancies, it seems to be generally agreed upon the fact that the magnitude of the TMP, the membrane pore size and the properties of the cells are major parameters in crossflow microfiltration. In order to gain more insight into these phenomena, however, a detailed study of the fluid mechanical aspects of crossflow filters, such as flow field characteristics, shear stress distribution, and fluidic movement of cells should be carried out. For instance, it has been shown that certain species of living cells are capable of a behaviour which is seemingly purposeful (Neidhardt et al., 1990; Kamm, 2002). In spite of the fact that they lack a nervous system, some bacteria species can swim away from unfavorable conditions, such as areas containing toxins or high mechanical stress. In vicinity of a solid wall, electrostatic, ionic and hydrodynamic forces have been found to affect bacterial motion. Correspondingly, some cells tend to move towards more favorable locations, such as areas with better supply of nutrients (Neidhardt et al., 1990). These types of responses to environmental conditions are termed taxis. It seems reasonable to assume that careful design of channel geometry, and thereby flow conditions, such that high wall shear stress near filtration outlets is achieved, should make it possible to take advantage of cell taxis in order to repel cells away from

the walls, and in that manner naturally counteract cell cake build-up and thereby reduce or avoid clogging and the resulting permeate flux reduction.

In order to perform such geometrical manipulation, the possibility to obtain detailed knowledge of the flow field characteristics inside a microfluidic device is of vital importance. For this purpose we have developed a micro-Particle Image Velocimetry (micro-PIV) system, which features low-cost while maintaining high accuracy, when compared to other micro-PIV setups. Micro-PIV is a whole-field, non-intrusive fluid flow measurement technique emerging from its macro-scale equivalent, PIV. Micro-PIV was first developed by Santiago et al. (1998). A year later, a modified version of this technique, using lasers for illumination, was illustrated by Meinhart et al. (1999). Although several publications reporting data acquired by means of micro-PIV exist in the literature today, limited information on crucial details concerning system set-up and design are available – information which is presented below.

MICRO-PIV SYSTEM

A schematic illustration of the micro-PIV system set-up is shown in fig. 1.

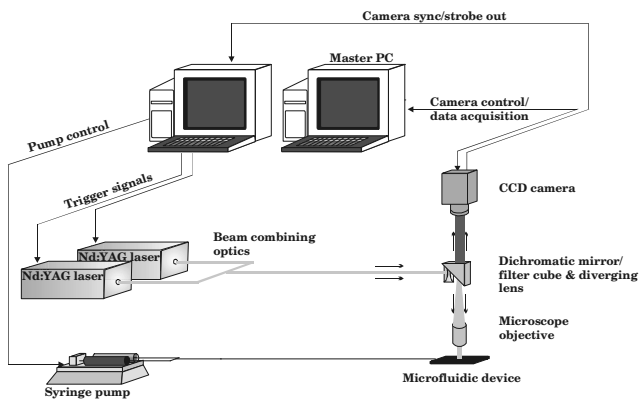


Fig. 1: Schematics of the micro-PIV system setup.

The system consists of two lasers, a microscope equipped with an epi-fluorescent filter cube, a CCD (Charge Coupled Device) camera for image recording, a syringe pump and two PC's for synchronization, acquisition and system control. The various system components are described in the following.

Seeding particles

De-ionized water was used as working fluid, seeded with 0.08% (per volume) fluorescent polymer microspheres manufactured by Duke Scientific Corporation. This particle concentration was selected as it

was found to be the maximum seeding load providing images with acceptably low noise levels under the current illumination conditions. The particle diameter was $1\mu\text{m}$ with a specific gravity of 1005 kg/m^3 . Particles loaded with a fluorescent dye with peak excitation wavelength $\lambda_{\text{ex}} = 540\text{nm}$ and peak emission wavelength $\lambda_{\text{em}} = 620\text{nm}$ were chosen for the experiment. The large Stokes' shift of the selected fluorescent dye permitted effective filtering of background reflections and noise from the illuminating lasers. A syringe pump (PHD2000 from Harvard Apparatus) was used to drive the seeded working fluid through the microfluidic device.

Lasers

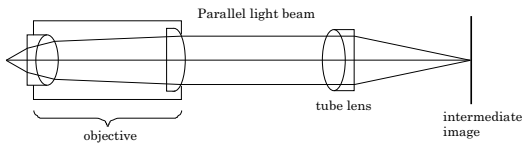
The fluid flow was illuminated by two pulsed Nd:YAG lasers (Minilite from Continuum), each with 5 ns pulse length. The lasers are optically connected by half-mirrors such that the beam from each laser exiting the system has the same direction and appears to originate from the same point in space. In this manner, the system acts as a double-pulsed laser. The laser beams are frequency-doubled at the exit resulting in pulse emissions with a wavelength of $\lambda = 532\text{ nm}$. The maximum pulse energy was 10mJ for both lasers. The laser system was mounted on a 0.7 by 0.7 m² optical table and positioned on an in-house made positioning stage permitting accurate adjustment of the exit beam relative the entrance aperture of the microscope. No optical fiber connections were applied.

Microscope

Imaging was performed via an up-right BX51 system microscope from Olympus equipped with a 20X planachromat objective lens and a fluorescence filter cube. The fluorescence filter cube was equipped with a dichromatic mirror to reflect the illuminating wavelength of 532 nm and a barrier longpass filter with a pass wavelength of 590 nm, i.e. allowing the fluorescent signal emitted from seed particles to pass. As the light source was monochromatic, no excitation filter was applied.

Microscope objective. The objective used for the current application is termed infinity-corrected, as most objectives available on today's market are. In an infinity-corrected optical system, the rear iris of the objective produces a parallel beam of light (focused to infinity; hence the term infinity-corrected) and the image is formed by a separate lens downstream the objective, the tube lens. In contrast, the finite-corrected system does not require a tube lens and the image is formed directly by the rear lens of the objective, see fig.2.

Infinity-corrected optical system:



Finite-corrected optical system:

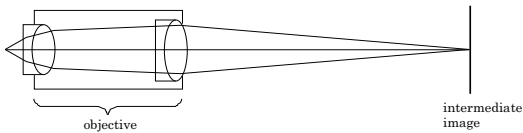
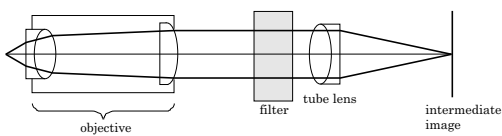


Fig. 2: Infinity corrected (top) and finite corrected (bottom) optical systems.

Infinity-corrected optical system:



Finite-corrected optical system:

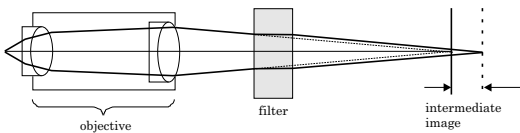


Fig. 3: Infinity-corrected (top) and finite-corrected (bottom) optical systems with a filter unit inserted in the light path.

When the microscope application requires intermediate optics or attachments, as is the case in micro-PIV, the properties of the infinity-corrected system provide two important advantages. First, in the infinity-corrected system, there is no change in magnification when the distance between the objective and tube lens is altered. This means that camera adapters, housings, etc. can be added to the system, and objectives can be switched between microscopes of different geometrical dimensions while preserving magnification. Second, the introduction of prisms, filters, etc. in the light path between the objective and the tube lens does not cause aberrations. The latter point is illustrated in fig. 3, where it is clearly seen that insertion of a filter unit in the light path of a finite-corrected system causes a displacement of

the intermediate image plane, while the infinity-corrected system remains unaffected.

Flow illumination. There is one important consequence of the application of infinity-corrected objectives in micro-PIV, namely that a collimated light beam can not be used for flow illumination. The beam is then focused to a single point in the objective's focal plane instead of illuminating the field of view of the microscope, see fig. 4a). Due to the high laser power, the focused beam may damage the microfluidic device. In order to achieve volume illumination, a lens with a negative focal length must be introduced in the light path up-stream the dichromatic mirror. In this way, the focal spot of the illuminating light created by the objective is shifted to a plane further away from the front lens, and does not coincide with the microscope's objective focal plane. Instead, the cone of laser light emerging from the objective's front lens is 'sliced' by the objective focal plane, thereby illuminating a portion of the microscope field of view, see fig. 4b).

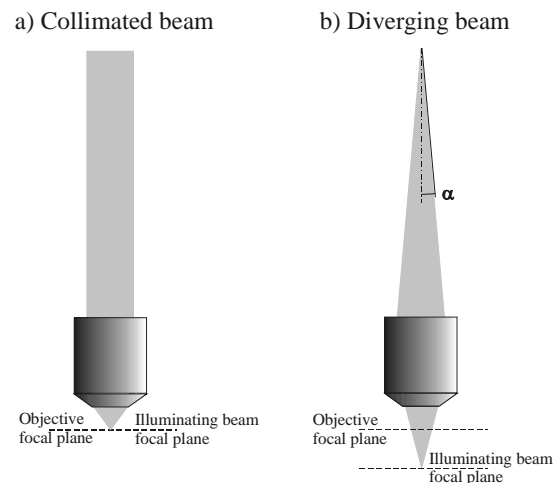


Fig. 4: a) Illumination by a collimated beam of light. The objective focal plane and beam focal plane overlap. No field illumination achieved. b) Illumination by a diverging beam of light. The focal plane of the illuminating beam is shifted to a plane further away from the objective, resulting in field illumination of the objective's focal plane.

The extent of the illuminated field depends on the the half-cone angle α of the beam entering the rear iris of the objective lens. The maximum achievable angle is in turn governed by the rear iris diameter and the distance between the concave lens and the objective. As no excitation filter was needed, a lens with a focal number $f = -20\text{mm}$ was mounted in the free space of the filter cube, directly upstream the dichromatic mirror. In this manner, the shortest possible distance between the

concave lens and rear iris of the objective was achieved. For the microscope in use, this distance was 107mm. With the diameter of the rear iris of the objective being 10mm, the half-cone angle α was 2.7° . The focal number of the concave lens was chosen such that the angle of the laser beam cone was slightly larger than the angle between the center of the lens and the edge of the rear iris of the microscope objective. In this manner, an evenly illuminated field, large enough to cover the entire area of the recording CCD array, was produced. The optical setup is shown in fig. 5.

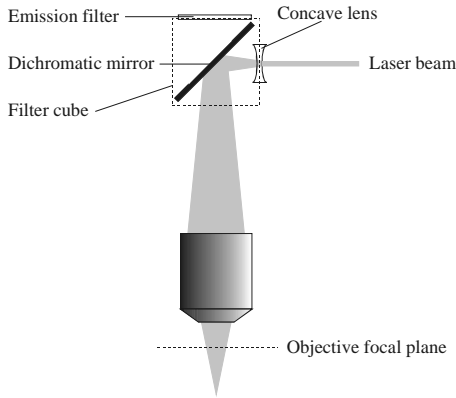


Fig. 5: Optical setup for flow illumination.

Visual field brightness. The visual field brightness, or *image brightness* (B) in an epi-fluorescent system is proportional to the ratio between the objective's numerical aperture NA to the fourth power and the square of its magnification factor M (Inoue and Spring, 1997):

$$B \propto \frac{NA^4}{M^2} \quad (1)$$

In micro-PIV, image brightness is an essential parameter due to the weak fluorescence intensity of the small tracer particles. By increasing the image brightness, smaller tracer particles can be imaged, and thus spatial resolution of the system may be increased. Equation (1) implies that the image brightness can be improved by selecting an objective with the highest possible NA while keeping low magnification. Often, however, the choice of objective becomes a practical trade-off between image brightness, field of view, and availability. The objective used for the current work had $NA = 0.40$ and $M = 20$, as it allowed to cover the desired portion of the flow field in one image.

Image recording

Images of the flow field were recorded using a Kodak MEGAPLUS ES/1.0 10bit CCD camera. This camera has

an active 1008×1018 pixel array with $9\mu\text{m}$ square pixels, and capability of recording images for cross-correlation with $1\mu\text{s}$ delay between frames, at a framerate of 15 image pairs per second. The images were transferred to a PC via a RoadRunner framegrabber from BitFlow. Due to the weak fluorescence signal, low objective image brightness, and rather low sensitivity and dynamic range of this camera compared with other cameras more frequently applied in micro-PIV, no particle images were visible on the raw recordings. However, by modification of the output Look Up Table (pixel value array) by defining a narrow range of white- and black cut-off pixel values and redistribution of these values over the entire 10bit gray level range, well-defined images of the fluorescent particles were achieved. Background noise from out-of-focus particles was dampened by taking an unfocused image of the flow field and subtracting it from the raw particle images prior to digital filtration.

Resolution and accuracy

Particle displacement. The resolution of any optical system is limited by diffraction (Inoue and Spring, 1997). In micro-PIV, this limit is posed by the diameter d_s of the central ring (Airy ring) in the diffraction pattern formed by the fluorescent particles. When imaging circular, self-luminous objects, the diameter of the point-spread function is given by:

$$d_s = 2.44M \frac{\lambda}{2NA} \quad (2)$$

where M is the magnification, λ is the wavelength and NA is the numerical aperture of the objective (Born and Wolf, 1999). With $M=20$, $NA = 0.4$ and $\lambda_{\text{em}} = 620\text{nm}$, the diameter of the point-spread function in the current experiment is $d_s \approx 37.8 \mu\text{m}$.

The diameter of the image recorded by the CCD array is a convolution of the diffraction-limited and geometrical image, and can be approximated by (Adrian, 1991):

$$d_e = \sqrt{(M^2 d_p^2 + d_s^2)} \quad (3)$$

where d_e is the effective image diameter and d_p is the particle diameter. With $d_p = 1\mu\text{m}$, the effective image diameter recorded by the CCD array in our experiment is $42.8 \mu\text{m}$, meaning that each particle was resolved by at least 4 pixels. This is sufficient resolution to ensure that the correlation peak may be determined within $1/10$ of the effective diameter (Prasad et al., 1992), i.e. $4.28 \mu\text{m}$. Projected back into the flow, this corresponds to a displacement error of approximately 210 nm in the measurement plane.

Measurement depth. The measurement depth of a micro-PIV system is defined by Meinhardt et al. (2000) as

twice the distance from the object plane to a location such that the imaged particle is sufficiently unfocused, and thus has low enough intensity, so that it does not significantly contribute to the velocity measurement. The particle image intensity when this occurs is set to 10% of the maximum intensity of a focused particle, yielding the following expression:

$$\delta z_m = \frac{3n\lambda_o}{NA^2} + \frac{2.16d_p}{\tan \theta} + d_p \quad (4)$$

where δz_m is the measurement depth, n is the refractive index of the imaging medium, λ_o is the wavelength of the imaged light in vacuum, and θ is the light collecting angle of the objective (Meinhart et al., 2000). By inserting the actual values into eq. (4), the measurement depth for our experiment is estimated to be $17.6 \mu\text{m}$.

Spatial resolution. The spatial resolution of a PIV experiment is determined by the size of the first interrogation window. $32 \text{ pixels} \times 64 \text{ pixels}$ (lateral and streamwise directions, respectively) interrogation regions were used in the current experiments. This corresponds to $14.4 \mu\text{m} \times 28.8 \mu\text{m}$ resolution in the measurement plane. Using a window overlap of 75% and 50%, respectively, a lateral vector spacing of $3.6 \mu\text{m}$ and $7.2 \mu\text{m}$ was achieved.

SINUSOIDAL CHANNEL EXPERIMENTS

A schematic drawing of the sinusoidal silicon channel and its dimensions is shown in fig. 6. The channel width at the narrowest cross-section (hereafter termed *w waist*) was $150 \mu\text{m}$, and $250 \mu\text{m}$ at the widest cross-section. The wave length of the sinusoidal wall was $105 \mu\text{m}$. The channel depth was approximately $50 \mu\text{m}$. The total length of the sinusoidal channel was 26 mm . The channel structure was mounted in a multi-layer housing allowing for fluidic connections and clamping. Both the channel and the housing were manufactured by IMM, Germany.

Measurements of the velocity field were performed approximately 20 mm downstream the channel entrance, in the central horizontal plane of the channel. This plane was found by focusing on the top and bottom walls, respectively, and then adjusting the microscope objective to a focal plane midway between the wall planes. The error in locating the central plane of the flowfield is estimated to be approximately $\pm 3 \mu\text{m}$. This error is mainly due to the focal depth of the optical system and the resolution of the vertical adjustment knob on the microscope stage.

As mentioned above, the seeding concentration in the current experiments was 0.08% (per volume), which was insufficient to perform direct interrogation on a single image pair while obtaining desired resolution. It is known that ensemble-averaging of individual correlation functions prior to peak detection may be applied in order

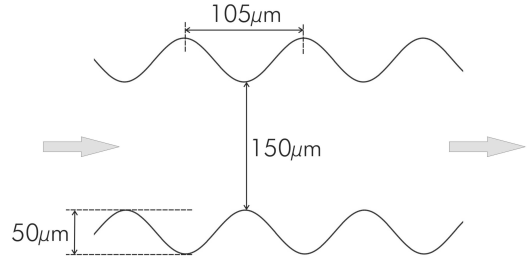


Fig. 6: Sinusoidal microchannel layout and dimensions.

to compensate for insufficient seeding and also to remove the random error introduced by Brownian motion of the seeding particles (Meinhart et al. 1999). In the current experiments, however, an ensemble averaging of individual image fields prior to interrogation was performed. The procedure was as follows: 16 double-frame realisations (32 single images), sampled at statistically independent times, were recorded. Then, all first-images from the 16 image pairs were added, resulting in a single, well-seeded first exposure image. The same procedure was applied to all second-images from the 16 image pairs. The two resulting images were then interrogated using standard interrogation schemes.

Two different flow cases were studied, one with $Re=2$ and one with $Re=10$, where Re is the Reynolds number defined as $Re=Uh/v$. The Re is here based on the average channel width h being $200 \mu\text{m}$.

RESULTS AND DISCUSSION

The velocity field for $Re=10$ inside the sinusoidal microchannel measured using the micro-PIV technique is shown in fig. 7 and 8. Figure 7 shows the entire flow field, while a blown-up detail of the flowfield near the wall is shown in figure 8. The centerline velocity is approximately 0.12 m/s .

The velocity profiles resulting from the micro-PIV measurements are presented in fig. 9 and 10 for the case $Re=2$ and $Re=10$, respectively. A theoretical solution for laminar flow between parallel plates of infinite width and separated by a distance corresponding to that of the smallest channel cross-section is plotted for the two cases for comparison (solid lines). The flatness of the measured velocity profiles near the channel center compared to the analytical solution is mainly due to the low aspect ratio of the channel used in the current experiments, i.e. the comparatively low channel depth.

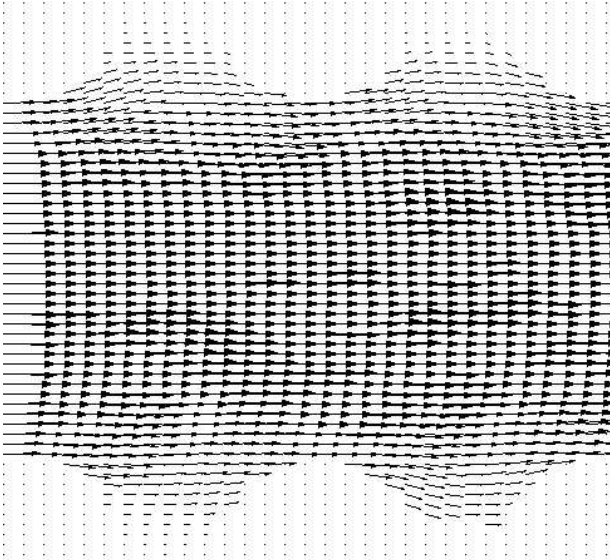


Fig. 7: Velocity field inside the sinusoidal microchannel, Re = 10.

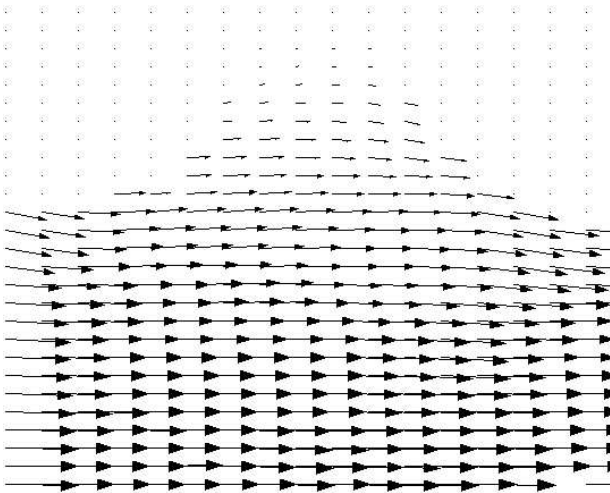


Fig. 8: Near-wall detail of velocity field, Re = 10.

As mentioned earlier, it is desirable to increase the wall shear stress in order to promote cell taxis away from the walls. The wall shear stress for a two-dimensional flow is defined as (White, 1991):

$$\tau_w = \mu \left(\frac{du}{dy} \right)_{wall} \quad (5)$$

where μ is the viscosity of the fluid and du/dy is the velocity gradient at the wall.

By inspecting fig. 9 and 10, it is clearly seen that the wall velocity gradient is higher at the waist of the sinusoidal channel compared to the theoretical parallel-plate solution for both Re cases. The wall shear stress for Re=2 was found to be approximately 1.4 times higher than for the corresponding straight-channel flow, and 1.6 times higher for the Re=10 case. It is reasonable to assume that the presence of these high-shear areas may promote shear-induced cell taxis toward the channel center more efficiently than a straight-wall geometry. When regarding a cross-flow filter, placing filter outlets in these areas (i.e. channel waists) might reduce problems arising from cell cake formation and clogging of such devices.

By comparing fig. 9 and 10, a distinct difference in the shape of the velocity profiles is found. For Re=2, the velocity profile at the widest channel cross-section is smooth and contains two single inflection point placed symmetrically around the centerline. For Re=10, the corresponding velocity profile contains several inflection points. The same feature is observed for the velocity profile at the channel waist for this Re. It is reasonable to assume that this effect is due to the sinusoidal shape of the channel imposing a periodic distortion on the flow field. This influence of channel shape is absent, or remarkably less distinct, in the low-Re flow. This, together with the earlier mentioned difference in shear ratio, implies that the flow field exhibits a dependence on the Reynolds number characterised by a change in flow characteristics occurring between Re=2 and Re=10.

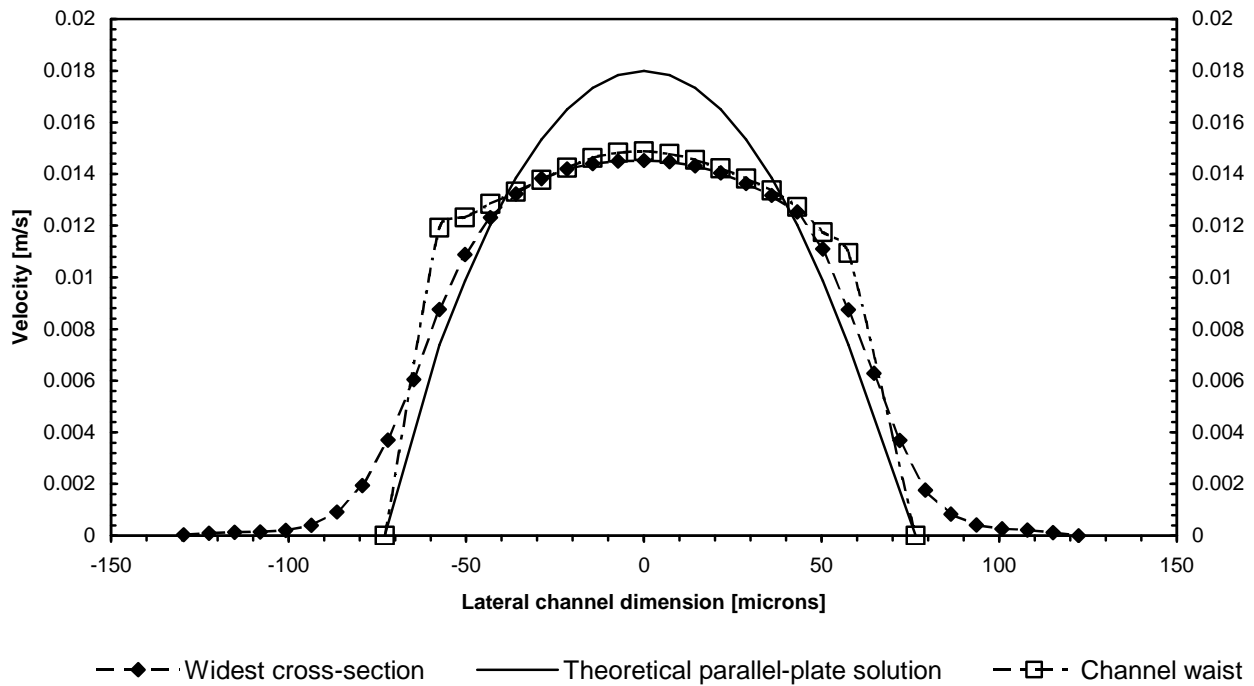


Fig. 9: Velocity profile at the waist (open squares) and the widest cross-section (tilted, filled squares) for $Re=2$. Parallel-plate solution (solid line) is presented for comparison.

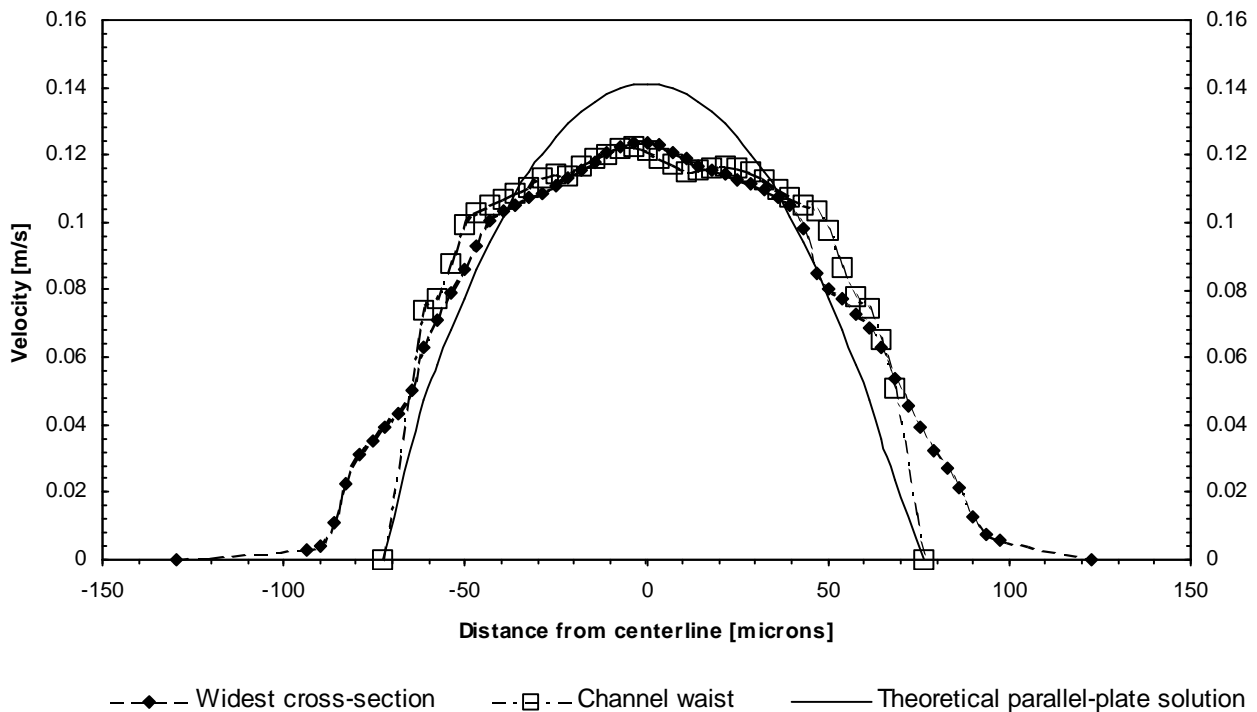


Fig. 10: Velocity profile at the waist (open squares) and the widest cross-section (tilted squares) for $Re=10$. Parallel-plate solution (solid line) is presented for comparison.

CONCLUSIONS

Micro-Particle Image Velocimetry (micro-PIV) is a measurement technique capable of providing high-resolution flow field measurements in microdevices. A micro-PIV system developed in our laboratories has been presented in detail, pointing out important aspects of micro-PIV system design crucial for its operation.

The micro-PIV system has been applied on a sinusoidal microchannel flow at two different Reynolds numbers, i.e. $Re=2$ and $Re=10$. It was found that the wall shear stress was increased by a factor of 1.4 and 1.6 compared to a parallel-plate flow for the low and high Re , respectively. It is therefore reasonable to assume that the presence of these high-shear areas will promote shear-induced motion of particles toward the channel center more efficiently than a straight-wall geometry. By placing fluid outlets in these areas for cross-flow filtration purposes, problems arising from clogging of such devices might be reduced.

The velocity profile for $Re=2$ at the widest channel cross-section was found to contain two inflection points symmetrically around the channel centerline, while several inflection points were found in the corresponding velocity profile for $Re=10$. This shows that the flow field under consideration exhibits a Reynolds number dependence, characterised by the onset of a periodic distortion in the velocity profile between $Re=2$ and $Re=10$. It is reasonable to assume that this distortion is imposed on the flow by the sinusoidal shape of the channel walls.

NOMENCLATURE

Latin Symbols

B – Visual field brightness [-]
 d_e – Effective particle diameter [m]
 d_p – Particle diameter [m]
 d_s – Point spread function diameter [m]
 d/dy – differential operator [1/m]
 f – Focal number [m]
 h – Channel width [m]
 M – Magnification factor [-]
 n – Refractive index [-]
 NA – Numerical Aperture [-]
 Re – Reynolds number [-]
 u – Instantaneous flow velocity [m/s]
 U – Mean flow velocity [m/s]

Greek Symbols

α – Half-cone beam angle [deg]
 δz_m – Measurement depth [m]
 λ – Wavelength of light [m]
 λ_{em} – Peak emission wavelength [m]
 λ_{ex} – Peak excitation wavelength [m]

λ_o – Wavelength of light in vacuum [m]
 μ – Dynamic viscosity [kg/(ms)]
 ν – Kinematic viscosity [m²/s]
 θ – Light collecting angle [deg]
 τ_w – Wall shear stress [N/m²]

ACKNOWLEDGEMENTS

This work is supported by The Research Council of Norway. The authors would also like to thank NorChip AS, Norway, and IMM, Germany, for valuable equipment support and cooperation.

REFERENCES

- Caridis, K.A., and Papathanasiou, T.D., 1997, Pressure effects in cross-flow microfiltration of suspensions of whole bacterial cells, *Bioprocess Engineering*, Vol. 16, pp. 199-208.
- Carrere, H., and Rene, F., 1998, Hydrodynamical behaviour of non Newtonian flows in a cross-flow filtration tubular module, *Experiments in Fluids*, Vol. 25, pp. 243-253.
- Kamm, R.D., 2002, Cellular Fluid Mechanics, *Annual Review of Fluid Mechanics*, Vol. 34, pp. 211-232.
- Meinhart, C.D., Wereley, S.T., Gray, M.H.B., 2000, Volume illumination for two-dimensional particle image velocimetry, *Meas. Sci. Technol.*, Vol. 11, pp. 809-814.
- Meinhart, C.D., Wereley, S.T., Santiago, J.G., 1999, PIV measurements of a microchannel flow, *Experiments in Fluids*, Vol. 27, pp. 414-419.
- Prasad, A.K., Adrian, R.J., Landreth, C.C., Offutt, P.W., 1992, Effects of resolution on the speed and accuracy of particle image velocimetry interrogation, *Experiments in Fluids*, Vol. 13, pp. 105-116.
- Santiago, J.G., Wereley, S.T., Meinhart, C.D., Beebe, D.J., Adrian, R.J., 1998, A particle image velocimetry system for microfluidics, *Experiments in Fluids*, Vol. 25, pp. 316-319.
- Born, M., and Wolf, E., 1999, *Principles of Optics*, 7th ed., Cambridge University Press, UK.
- Inoue, S., and Spring, R.K., 1997, *Video Microscopy: The Fundamentals*, 2nd ed., Plenum Press, New York.
- White, F.M., 1991, *Viscous Fluid Flow*, 2nd ed., McGraw-Hill.